Quantum computation of molecular geometry via many-body nuclear spin echoes

C. Zhang[#],[1] R. G. Cortiñas[#],[2] A. H. Karamlou[#],[2] N. Noll,[2] J. Provazza,[3] J. Bausch,[4] S. Shirobokov,[4] A. White,[2,3] M. Claassen,[2,5] S. H. Kang,[1] A. W. Senior,[4] N. Tomašev,[4] J. Gross,[2] K. Lee,[2] T. Schuster,[2,6] W. J. Huggins,[2] H. Celik,[1] A. Greene,[2] B. Kozlovskii,[4] F. J. H. Heras,[4] A. Bengtsson,[2] A. Grajales Dau,[2] I. Drozdov,[2,7] B. Ying,[2] W. Livingstone,[2] V. Sivak,[2] N. Yosri,[2] C. Quintana,[2] D. Abanin,[2] A. Abbas,[2] R. Acharya,[2] L. Aghababaie Beni,[2] G. Aigeldinger,[2] R. Alcaraz,[2] S. Alcaraz,[2] T. I. Andersen,[2] M. Ansmann,[2] F. Arute,[2] K. Arya,[2] W. Askew,[2] N. Astrakhantsev,[2] J. Atalaya,[2] B. Ballard,[2] J. C. Bardin,[2,8] H. Bates,[2] M. Bigdeli Karimi,[2] A. Bilmes,[2] S. Bilodeau,[2] F. Borjans,[2] A. Bourassa,[2] J. Bovaird,[2] D. Bowers,[2] L. Brill,[2] P. Brooks,[2] M. Broughton,[2] D. A. Browne,[2] B. Buchea,[2] B. B. Buckley,[2] T. Burger,[2] B. Burkett,[2] J. Busnaina,[2] N. Bushnell,[2] A. Cabrera,[2] J. Campero,[2] H.-S. Chang,[2] S. Chen,[2] Z. Chen,[2] B. Chiaro,[2] L.-Y. Chih,[2] A. Y. Cleland,[2] B. Cochrane,[2] M. Cockrell,[2] J. Cogan,[2] R. Collins,[2] P. Conner,[2] H. Cook,[2] W. Courtney,[2] A. L. Crook,[2] B. Curtin,[2] S. Das,[2] M. Damyanov,[2] D. M. Debroy,[2] L. De Lorenzo,[2] S. Demura,[2] L. B. De Rose,[2] A. Di Paolo,[2] P. Donohoe,[2] A. Dunsworth,[2] V. Ehimhen,[2] A. Eickbusch,[2] A. M. Elbag,[2] L. Ella,[2] M. Elzouka,[2] D. Enriquez,[2] C. Erickson,[2] V. S. Ferreira,[2] M. Flores,[2] L. Flores Burgos,[2] E. Forati,[2] J. Ford,[2] A. G. Fowler,[2] B. Foxen,[2] M. Fukami,[2] A. W. L. Fung,[2] L. Fuste,[2] S. Ganjam,[2] G. Garcia,[2] C. Garrick,[2] R. Gasca,[2] H. Gehring,[2] R. Geiger,[2] É. Genois,[2] W. Giang,[2] C. Gidney,[2] D. Gilboa,[2] J. E. Goeders,[2] E. C. Gonzales,[2] R. Gosula,[2] S. J. de Graaf,[2] D. Graumann,[2] J. Grebel,[2] J. Guerrero,[2] J. D. Guimarães,[2] T. Ha,[2] S. Habegger,[2] T. Hadick,[2] A. Hadjikhani,[2] M. P. Harrigan,[2] S. D. Harrington,[2] J. Hartshorn,[2] S. Heslin,[2] P. Heu,[2] O. Higgott,[2] R. Hiltermann,[2] J. Hilton,[2] H.-Y. Huang,[2] M. Hucka,[2] C. Hudspeth,[2] A. Huff,[2] E. Jeffrey,[2] S. Jevons,[2] Z. Jiang,[2] X. Jin,[2] C. Joshi,[2] P. Juhas,[2] A. Kabel,[2] H. Kang,[2] K. Kang,[2] R. Kaufman,[2] K. Kechedzhi,[2] T. Khattar,[2] M. Khezri,[2] S. Kim,[2] R. King,[2,9] O. Kiss,[2] P. V. Klimov,[2] C. M. Knaut,[2] B. Kobrin,[2] F. Kostritsa,[2] J. M. Kreikebaum,[2] R. Kudo,[2] B. Kueffler,[2] A. Kumar,[2] V. D. Kurilovich,[2] V. Kutsko,[2] N. Lacroix,[2] D. Landhuis,[2] T. Lange-Dei,[2] B. W. Langley,[2] P. Laptev,[2] K.-M. Lau,[2] L. Le Guevel,[2] J. Ledford,[2] J. Lee,[2] B. J. Lester,[2] W. Leung,[2] L. Li,[2] W. Y. Li,[2] M. Li,[2] A. T. Lill,[2] M. T. Lloyd,[2] A. Locharla,[2] D. Lundahl,[2] A. Lunt,[2] S. Madhuk,[2] A. Maiti,[2] A. Maloney,[2] S. Mandra,[2] L. S. Martin,[2] O. Martin,[2] E. Mascot,[2] P. Masih Das,[2] D. Maslov,[2] M. Mathews,[2] C. Maxfield,[2] J. R. McClean,[2] M. McEwen,[2] S. Meeks,[2] K. C. Miao,[2] R. Molavi,[2] S. Molina,[2] S. Montazeri,[2] C. Neill,[2] M. Newman,[2] A. Nguyen,[2] M. Nguyen,[2] C.-H. Ni,[2] M. Y. Niu,[2] L. Oas,[2] R. Orosco,[2] K. Ottosson,[2] A. Pagano,[2] S. Peek,[2] D. Peterson,[2] A. Pizzuto,[2] E. Portoles,[2] R. Potter,[2] O. Pritchard,[2] M. Qian,[2] A. Ranadive,[2] M. J. Reagor,[2] R. Resnick,[2] D. M. Rhodes,[2] D. Riley,[2] G. Roberts,[2] R. Rodriguez,[2] E. Ropes,[2] E. Rosenberg,[2] E. Rosenfeld,[2] D. Rosenstock,[2] E. Rossi,[2] D. A. Rower,[2] M. S. Rudolph,[2] R. Salazar,[2] K. Sankaragomathi,[2] M. C. Sarihan,[2] K. J. Satzinger,[2] M. Schaefer,[2,10] S. Schroeder,[2] H. F. Schurkus,[2] A. Shahingohar,[2] M. J. Shearn,[2] A. Shorter,[2] N. Shutty,[2] V. Shvarts,[2] S. Small,[2] W. C. Smith,[2] D. A. Sobel,[2] R. D. Somma,[2] B. Spells,[2] S. Springer,[2] G. Sterling,[2] J. Suchard,[2] A. Szasz,[2] A. Sztein,[2] M. Taylor,[2] J. P. Thiruraman,[2] D. Thor,[2] D. Timucin,[2] E. Tomita,[2] A. Torres,[2] M. M. Torunbalci,[2] H. Tran,[2] A. Vaishnav,[2] J. Vargas,[2] S. Vdovichev,[2] G. Vidal,[2] C. Vollgraff Heidweiller,[2] M. Voorhees,[2] S. Waltman,[2] J. Waltz,[2] S. X. Wang,[2] B. Ware,[2] J. D. Watson,[2] Y. Wei,[2] T. Weidel,[2] T. White,[2] K. Wong,[2] B. W. K. Woo,[2] C. J. Wood,[2] M. Woodson,[2] C. Xing,[2] Z. J. Yao,[2] P. Yeh,[2] J. Yoo,[2] E. Young,[2] G. Young,[2] A. Zalcman,[2] R. Zhang,[2] Y. Zhang,[2] N. Zhu,[2] N. Zobrist,[2] Z. Zou,[2] G. Bortoli,[2] S. Boixo,[2] J. Chen,[2] Y. Chen,[2] M. Devoret,[2,10] M. Hansen,[2] C. Jones,[2] J. Kelly,[2] P. Kohli,[4] A. Korotkov,[2] E. Lucero,[2] J. Manyika,[11] Y. Matias,[11] A. Megrant,[2] H. Neven,[2] W. D. Oliver,[2] G. Ramachandran,[2] R. Babbush,[2] V. Smelyanskiy,[2] P. Roushan,[2] D. Kafri,[2] R. Sarpong,[1] D. W. Berry,[12] C. Ramanathan,[13] X. Mi,[2,*] C. Bengs,[1,14,15,†] A. Ajoy,[1,14,16,‡] Z. K. Minev,[2,§] N. C. Rubin,[2,¶] and T. E. O'Brien[2,**]

[1] *Department of Chemistry, University of California, Berkeley, Berkeley, CA, USA*
[2] *Google Quantum AI, Santa Barbara, CA, USA*
[3] *Quantum Simulation Technologies Inc., Boston, MA, USA*
[4] *Google Deepmind, London, United Kingdom*
[5] *Department of Physics and Astronomy, University of Pennsylvania, PA, USA*
[6] *California Institute of Technology, Pasadena, CA, USA*
[7] *Department of Physics, University of Connecticut, Storrs, CT, USA*
[8] *USA Department of Electrical and Computer Engineering, University of Massachusetts, Amherst, MA, USA*
[9] *Simons Institute for the Theory of Computing, Berkeley, CA, USA*
[10] *Department of Physics, University of California, Santa Barbara, CA, USA*
[11] *Google Research, Mountain View, CA, USA*
[12] *School of Mathematical and Physical Sciences, Macquarie University, Sydney, Australia*
[13] *Department of Physics and Astronomy, Dartmouth College, Hanover, NH, USA*
[14] *Chemical Sciences Division, Lawrence Berkeley National Laboratory, Berkeley, CA, USA*
[15] *School of Chemistry, University of Southampton, Southampton, UK*
[16] *CIFAR Azrieli Global Scholars Program, Toronto, ON, Canada*

Quantum-information-inspired experiments in nuclear magnetic resonance spectroscopy may yield a pathway towards determining molecular structure and properties that are otherwise challenging to learn. We measure out-of-time-ordered correlators (OTOCs) [1–4] on two organic molecules suspended in a nematic liquid crystal, and investigate the utility of this data in performing structural learning tasks. We use OTOC measurements to augment molecular dynamics models, and to correct for known approximations in the underlying force fields. We demonstrate the utility of OTOCs in these models by estimating the mean ortho-meta H-H distance of toluene and the mean dihedral angle of 3',5'-dimethylbiphenyl, achieving similar accuracy and precision to independent spectroscopic measurements of both quantities. To ameliorate the apparent exponential classical cost of interpreting the above OTOC data, we simulate the molecular OTOCs on a Willow superconducting quantum processor, using AlphaEvolve-optimized [5] quantum circuits and arbitrary-angle fermionic simulation gates. We implement novel zero-noise extrapolation techniques based on the Pauli pathing model of operator dynamics [4], to repeat the learning experiments with root-mean-square error 0.05 over all circuits used. Our work highlights a computational protocol to interpret many-body echoes from nuclear magnetic systems using low resource quantum computation.

Accurate molecular structure determination is key to probing structure-function relationships in many areas of chemistry and biology. Nuclear Magnetic Resonance (NMR) spectroscopy provides access to structurally rich information embedded within couplings between pairs of spins [6]. Dipolar couplings in solid-like systems provide the most direct access to geometric information. However, the complex spin dynamics generated by these terms increases the challenge of observing [7] and interpreting [8, 9] an information-containing signal. Current techniques to overcome these challenges [10–14] focus on reducing the effective system size to one or a few spins, where signals remain large and interpretable. This has been pivotal in structural elucidation efforts, ranging from model systems in solid state [15, 16] and liquid crystal [17, 18] to complex, biologically relevant targets such as amyloid fibrils[19, 20] and SARS-CoV-2 [21]. A methodological gap remains however, as these techniques limit the maximum measurable distance between pairs of spins (e.g. C-C distances are limited to around ∼6Å. [22]), and longer-range distance constraints remain more challenging to estimate.

Efficient simulation of many-body spin dynamics, such as in NMR [23–29], has been suggested as an application for quantum computers. For quantum applications, one targets observables that do not concentrate [30–32] and that are sensitive to microscopic system details [4]. In this work, we propose that this sensitivity is relevant to the NMR practitioner, as quantum-information-inspired experiments could provide access to long range structural information. Recent efforts have demonstrated quantum advantage in the estimation of out-of-time-ordered correlators (OTOCs) [1, 2, 33] on superconducting quantum hardware [4]. The OTOC experiment is based on a many-body echo, in which polarization initially localized on a target spin migrates through the spin network, before a Hamiltonian-engineered time-reversal refocuses to the initial state. This refocusing is sensitive to perturbations on distant butterfly spins, which allows one to measure the extent of polarization propagation through the spin network [Fig. 1(a-b)]. We suggest this may help to fill the aforementioned NMR methodological gap.

Herein, we demonstrate a pathway towards determining otherwise challenging-to-compute molecular structure and properties via a hybrid technique of NMR spectroscopy and digital quantum simulation [Fig. 1(c)]. We measure OTOCs generated by Hamiltonian-engineered pulse sequences on ^{13}C-labeled organic molecules, [4-^{13}C]-toluene and [1-^{13}C]-3',5'-dimethylbiphenyl (DMBP), which we suspend in liquid crystal solvents to suppress intermolecular couplings while partially retaining intramolecular through-space dipolar terms. We compare experimentally obtained OTOCs from toluene to classical simulations using reference data, and illustrate the sensitivity of OTOCs to molecular structure by simulating stretching the molecule between the ortho and meta carbon atoms, yielding an interpretable NMR signal. To alleviate the exponential-scaling simulation cost of this approach, we repeat the above analysis on superconducting quantum hardware. We compile a Trotterized approximation of the all-to-all dipolar Hamiltonian evolution to a swap network of arbitrary-angle fermionic simulation (fSim) gates, and develop novel error mitigation techniques based on the Pauli-path picture of operator dynamics to recreate the learning experiment with high accuracy. Next, we demonstrate a DMBP structure learning protocol by combining NMR OTOC data with a realistic model obtained through classical molecular dynamics to estimate the distribution of the dihedral angle between the two phenyl rings. We use the AlphaEvolve coding agent to optimize product formula generation, and implement the resulting circuits on the quantum device. We compare the resulting estimates of the dihedral angle distribution against multiple quantum coherence (MQC) spectroscopy data from an independent DMBP sample with deuterated methyl groups, experimentally validating the OTOC learning protocol through a secondary

* mixiao@google.com
† c.bengs@soton.ac.uk
‡ ashokaj@berkeley.edu
§ zminev@google.com
¶ nickrubin@google.com
** teobrien@google.com
# These authors contributed equally to this work.

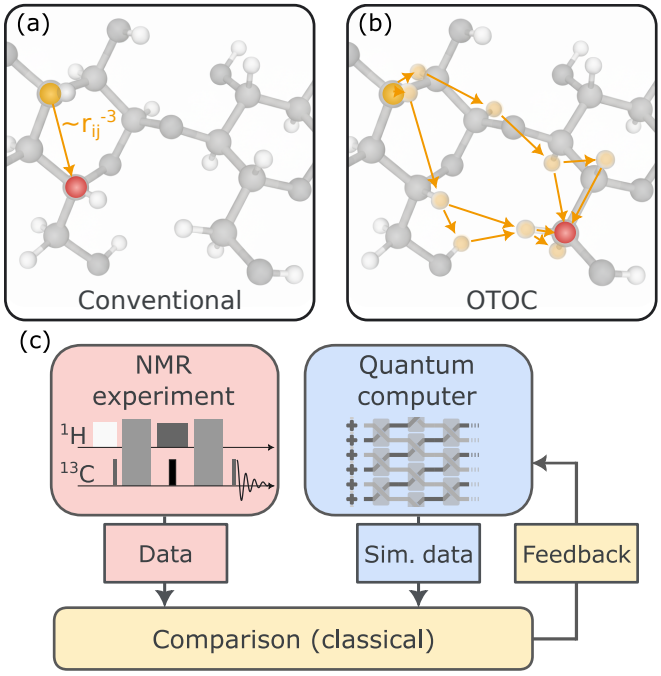

FIG. 1. **Making a longer molecular ruler with an out-of-time-ordered correlator (OTOC).** a,b) A comparison between conventional spin transport measurements that infer distance restraints from single couplings, and OTOC measurements, which probe the growth of large quantum coherences through the H spin network. By utilizing all the couplings in the spin network, the OTOC is not limited in distance by the $1/r^3$ scaling that limits the distances measurable by conventional techniques. c) Our proposal to use a quantum computer to assist in processing OTOC (or other challenging-to-classically-simulate) data from a large spin cluster. Following nuclear magnetic resonance (NMR) data collection, the quantum computer provides an artificial system that is iteratively tuned —via classical feedback— until it matches experiment.

unscalable spectroscopic approach. The combination of careful hardware error-mitigation, algorithmic compilation strategies, and physical chemistry model construction demonstrates the potential of scalable quantum-information-inspired experiments to augment traditional NMR data used for structure determination.

RESULTS

We illustrate in Fig. 2(a-b) the encoding of long-range correlations in an NMR experiment using a sample of [4-^{13}C]-toluene in N-(4-Ethoxybenzylidene)-4-butylaniline (EBBA) liquid crystal as a benchmark system with externally determinable molecular structure. We perform experiments using the newly-developed Time-Accurate Reversal of Dipolar InteractionS (TARDIS) pulse scheme, that engineers an effective double-quantum Hamiltonian to propagate information between the x-polarized ^{13}C "measurement" spin and the methyl proton "butterfly" spins. Due to symmetries in the double-quantum Hamiltonian, the TARDIS sequence is approximately invertible, allowing us to refocus the propagated information back to the ^{13}C spin, which is reflected in the amplitude of the free induction decay (FID). In the absence of any perturbation between forward and backward evolution this sequence performs a Loschmidt Echo (LE) on the system [Fig. 2(c), yellow]. In principle this LE sequence should yield a constant signal, corresponding to perfect refocusing. The observed decay is partially due to higher order Hamiltonian terms in the static effective expansion that are imperfectly refocused, and partially due to inhomogeneities in the applied radio frequency (RF) field across the NMR sample (see Supplementary Information for detailed modeling).

To determine the information spread through the toluene molecule during forward evolution, we apply a "butterfly" unitary operation on the methyl group before refocusing. This yields an OTOC [Fig. 2(c), red], which in the absence of error takes the functional form

$$C(t) = \mathrm{Trace}[X_{^{13}\mathrm{C}}(t)\, B\, X_{^{13}\mathrm{C}}(t)\, B^\dagger], \qquad (1)$$

where $X_{^{13}\mathrm{C}}(t) = U(t)X_{^{13}\mathrm{C}}U^\dagger(t)$ is the forward-evolved measurement operator. At short times the ^{13}C spin remains undisturbed by the distant butterfly; the OTOC matches the LE. However, as the spin spreads across the system the butterfly effect grows, and the OTOC decays faster than the LE. This decay is characteristic of all OTOCs: the information from the measurement spin propagates with a diffusive front, and causes decay upon reaching the butterfly.

The onset and rate of the OTOC decay depends on the dipolar couplings, enabling determination of a model molecular structure corresponding to the thermal average of all molecular configurations. Due to the simplicity and symmetry of toluene, this average structure can be well approximated by a rigid phenyl ring and a freely-rotating methyl group [34]. The liquid crystal environment can be accounted for by an orientational order parameter. We model OTOCs generated by the exact TARDIS pulse sequence, and include independently-measured RF inhomogeneity. Then, for illustrative purposes, we can simulate an artificial stretching of the molecule between the ortho- and meta- positions [Fig. 2(d), inset], measured by the ortho-meta H-H distance z_{om}. This affects the OTOC decay strongly [Fig. 2(d)]: we observe that a stretch or contraction of 0.5Å shifts the OTOC by up to 20%. The direction of this shift is counterintuitive: decreasing z_{om} (which increases coupling strengths) slows the OTOC at later times. We explain this observation in the Supplementary Information.

To turn the OTOC sensitivity into a tool for learning molecular structure, we construct a cost function to minimize over our target parameter z_{om}. In Fig. 2(e) we plot the covariance-weighted error to the data from Fig. 2(c) and 4 other datasets generated by engineering an on-site field (see Supplementary Information). Performing a cubic fit and bootstrapping error bars, we obtain an

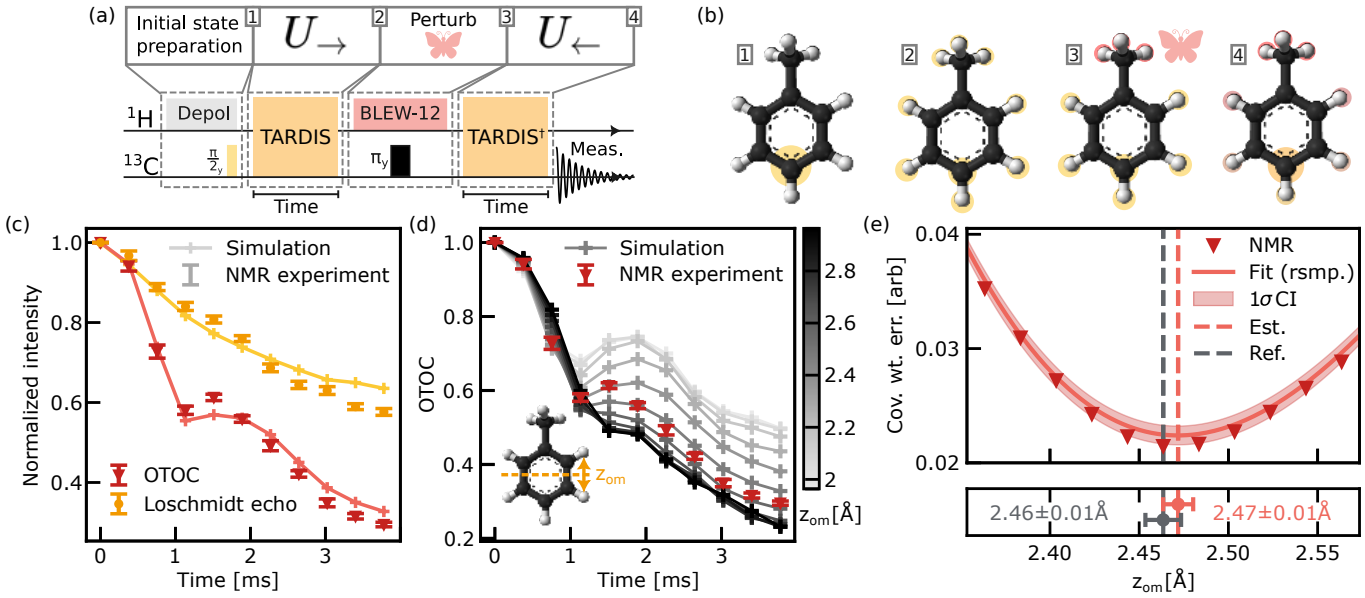

FIG. 2. **Benchmarking the structural sensitivity of out-of-time-ordered correlators (OTOCs) in [4−^{13}C]-toluene.** a) Description of the OTOC protocol (top) as implemented in a nuclear magnetic resonance (NMR) spectrometer (bottom). b) Cartoon showing the spread of the spin cluster through the molecule following the sequence in a). c) OTOC (red) and Loschmidt echo data (yellow) from the NMR experiment. Points show NMR experiment data with 1σ confidence intervals (CI), compared to numerical simulations (lines). d) Sensitivity of the OTOC experiment to an artificial stretch of benzene between the ortho and meta carbon atoms (inset), with experimental data from b) overlaid (red). e) Simulated learning of the ortho-meta H-H distance z_{om} from OTOC data. (top) Red triangles show the covariance weighted mean error between simulation and NMR experiment, line shows a cubic fit with 1σ CI shaded. (bottom) Estimate of z_{om} (red) compared to reference data from the literature (gray), with bootstrapped 2σ CI.

estimate $z_{\mathrm{om,\,c}} = 2.47 \pm 0.01$ Å. This agrees with the reference value $z_{\mathrm{om,\,r}} = 2.46 \pm 0.01$ Å [34] to within error bars, and shows comparable precision to this reference data. We caution however that this fits only a single parameter of the entire toluene molecule, whilst Ref. [34] fits the entire molecular structure.

The classical hardness of OTOC simulation prevents scaling our structure learning protocol to larger systems of chemical and biological interest using classical post-processing alone. We ameliorate this issue by efficiently simulating the strongly correlated dipolar coupling Hamiltonian on superconducting quantum hardware, implementing the scheme envisaged in Fig. 1(c). Compared to established applications in quantum simulation of electronic structure, OTOC simulation is a relatively low-cost application for quantum computers due to short scrambling timescales, low measurement complexity, and large error tolerances. However, the all-to-all-coupled dipolar spin Hamiltonian is challenging to simulate compared to local spin models, due to the large number of terms. To solve this problem, we implement a first-order Trotterization [35] of the lowest-order Magnus expansion of the full TARDIS sequence, working in the interaction picture [36] on the ^{13}C-para-H coupling, and neglecting all other C-H couplings. We compile the H-H interactions into a swap network [37], and implement the resulting fSim gate in an individually calibrated two-pulse scheme [Fig. 3(a)]. The resulting circuits use up to 1080 2-qubit pulses to simulate the first six time steps of the toluene OTOC curve. We further develop a physically motivated zero-noise extrapolation scheme [38, 39] based on the effect of noise in the Pauli-path OTOC picture [4, 26].

In Fig. 3, we repeat the sensitivity experiment across the range of z_{om} shown in Fig. 2(c), but replacing the classical computation with quantum simulation performed on a Willow device. We observe that the quantum device is able to qualitatively replicate the OTOC decay across the z_{om} range considered. Comparing our hardware to the classical simulation of Fig. 2(c), we find a root-mean-square error between the quantum and classical datasets of $\epsilon_{\mathrm{tot}} = 0.058$. This is made up of algorithmic error (i.e. Trotter error) in the quantum circuit ($\epsilon_{\mathrm{alg}} = 0.035$) and residual experimental bias after mitigation ($\epsilon_{\mathrm{exp}} = 0.050$). In the Supplementary Information, we provide detailed budgeting of the algorithmic, NMR, and quantum computer error sources. Motivated by the accuracy in replicating the OTOC decay on quantum hardware, we reproduce the covariance-weighted error curve [Fig. 3(c), blue], and re-estimate the ortho-meta C-C bond length. We observe that the dip remains, and obtain an estimate $z_{\mathrm{om,\,q}} = 2.44 \pm 0.04$ Å, which suffers a small loss of precision, but continues to agree with the reference data within experimental error. To separate the effect of the reduced dataset from the algorithmic and experimental error, we repeat this plot using the ac-

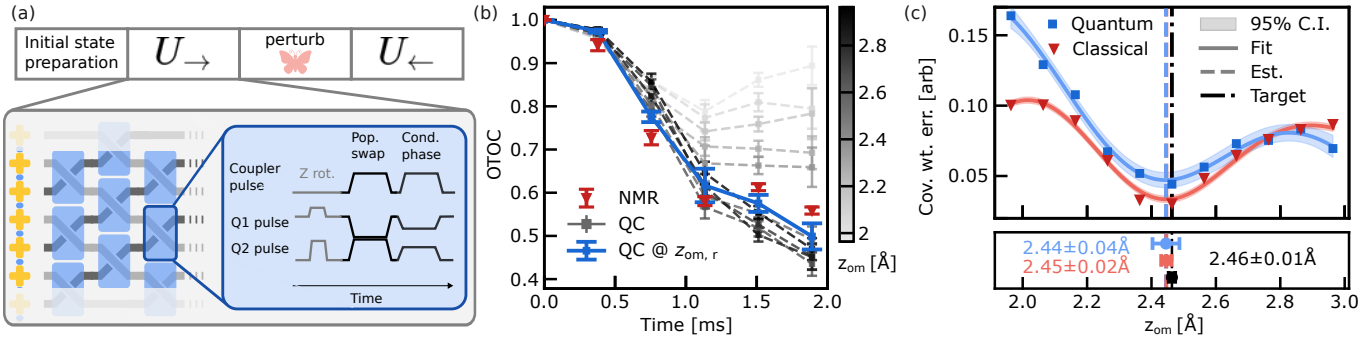

FIG. 3. **Alleviating the exponential cost of out-of-time-ordered correlator (OTOC) simulation with a quantum computer.** a) Approximating nuclear spin evolution on superconducting quantum hardware. A Trotterized digital quantum simulation of the double quantum Hamiltonian is executed by compiling individual couplings with swap gates that permute spin indices. The compiled gate is executed using a pulse train divided into a Z rotation, partial population swap, and conditional phase gate. b) Error-mitigated simulations of the first five points of the OTOC curve on quantum hardware, swept over the same range of ortho-meta C-C bond lengths $z_{\rm om}$ as in Fig. 2(c). The target simulation at $z_{\rm om,\,r} = 2.46$ Å is emphasized (solid blue line), error bars are 1σ confidence intervals (CI). c) (upper) Comparison of the learning experiment using quantum and classical data. Fits (lines) are from a bootstrapped Gaussian process regression, with 1σ CI shaded. (lower) Comparison of two estimates of $z_{\rm om}$ to reference data, with bootstrapped 2σ CI.

curate classical simulation from Fig. 2, but using only the first 5 points of the OTOC [Fig. 3(c), red], achieving an estimate $z_{\rm om,\,c-} = 2.45 \pm 0.02$ Å. The loss of precision in the quantum calculation thus comes partially from the smaller dataset used, and partially from a mix of algorithmic and experimental error.

To demonstrate an OTOC based learning protocol on degrees of freedom common to chemical systems, we perform a learning experiment focusing on the biphenyl dihedral angle ϕ of DMBP dissolved in 4-Cyano-4'-pentylbiphenyl (5CB). The energy barrier to this rotation is sufficient to prevent completely free spinning, but the barrier is insufficient to make the structure rigid at experimental temperatures and pressure, so we consider an ensemble of ϕ angles. This distribution is not precisely captured by molecular dynamics with an approximate molecular mechanics force-field (MD/MM), nor with high-level vacuum electronic structure simulations. However, of the intramolecular degrees of freedom of the DMBP molecule, the phenyl and methyl bond distances are too rigid to be significantly affected by the interaction with the liquid crystal environment, whilst the methyl torsions are too unconstrained to be affected by this environment. We can leverage this by capturing the rigid rotations using MD/MM, and re-parameterizing our model such that only the dihedral angle contributions remain.

Our task is thus to learn the free energy surface, or potential of mean-force PMF(ϕ) [Fig. 4(b)], along the dihedral angle ϕ. This yields the dipolar couplings via Boltzmann's distribution: $D_{ij} = \int d\phi \exp[-\beta\ \mathrm{PMF}(\phi)] D_{ij}(\phi) / \int d\phi \exp[-\beta\ \mathrm{PMF}(\phi)]$, with β the inverse temperature. We capture the ϕ-dependent couplings $D_{ij}(\phi)$ by binning and averaging MD trajectories as separated by this collective variable. Then, we take a simple sinusoidal model with a few free parameters, and interpolate between estimates from MD/MM, an artificial shifted double well potential, and a vacuum phase DFT torsion scan. This yielded 9 candidate PMFs (Fig. 4(b)), of which the MD/MM estimate corresponds to a PMF with minimum at $\phi = 32.4°$, the DFT estimate corresponds to a PMF with minimum at $\phi = 41.8°$, and the artificial double well with a corresponding PMF minimum at $\phi = 50^o$.

The learning task can be accomplished by simulating the OTOCs for these candidate PMFs on a Willow quantum chip and selecting the candidate PMF that minimizes the difference between the simulated and experimentally measured OTOC curves. To generate quantum circuits that match the numerical verification of TARDIS, we use exponentially-costing exact simulation and the AlphaEvolve coding agent to evolve a first-order Trotter formula generator and produce a novel product formula algorithm. This achieves a low mean error (0.0084) to the exact OTOC simulation across the entire PMF range, using no more than 792 CZ gates.

We show the learning experiment on the quantum device in Fig. 4(d), using the first 2.5 ms of NMR data for the quantum simulation (blue, QC), and the entire 4 ms decay curve for a comparative classical simulation (red, sim.) that includes accurate modeling of the RF inhomogeneity. The quantum computer achieves an RMSE of 0.05 to exact simulation of the input circuits across the entire range of data, matching the performance of the toluene example. The minima of the two cost functions agree within error bars, $\phi_{\rm QC} = 40° \pm 3°$, whilst $\phi_{\rm sim} = 41.5° \pm 0.2°$. In Fig. 4(c) we plot the OTOC for the QC simulation of the nearest PMF, with NMR experimental data and classical simulations overlaid.

To confirm the OTOC prediction of the dihedral angle model, we simulate MQC spectra from a partially deuterated DMBP sample [(1-^{13}C)-3',5'-bis(methyl-d$_3$)biphenyl] using the 9 PMFs, and compare

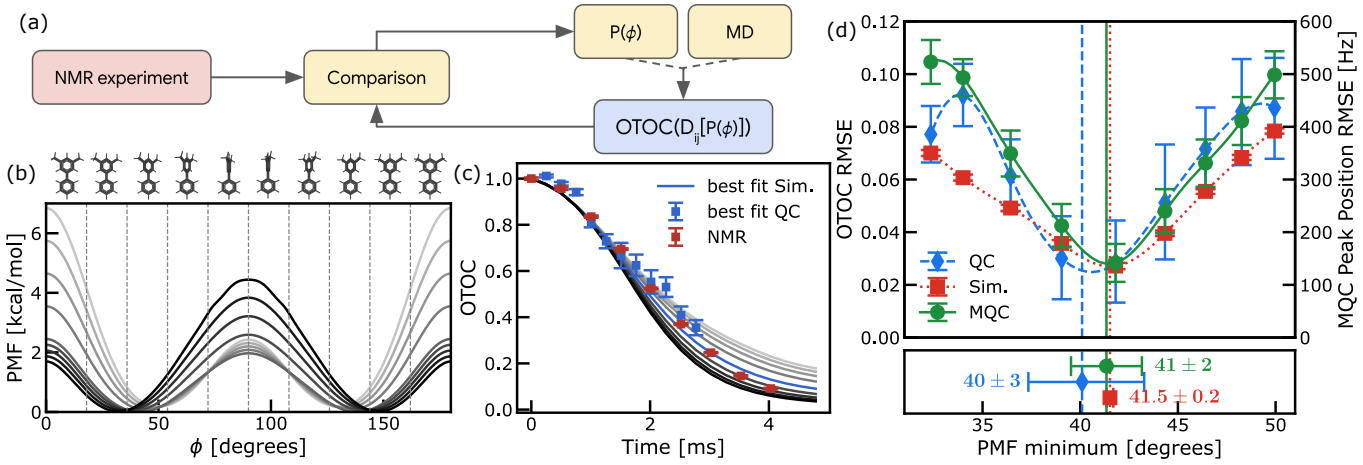

FIG. 4. **Refining a molecular mechanics model of the torsion free energy of [1-^{13}C]-3',5'-dimethylbiphenyl (DMBP), validated by multiple quantum coherence (MQC) experiments.** a) Workflow diagram identifying whether a task is performed in the nuclear magnetic resonance spectrometer (red), on the quantum computer (blue), or classically (yellow). b) Plots of the 9 potential of mean-force (PMF) candidate functions of the dihedral angle of DMBP. c) Out of time ordered correlators (OTOC) of DMBP, comparing experimental NMR data (red points), OTOC simulations run on the Willow chip using the most likely PMF (blue points), and classical simulations with added RF inhomogeneity (lines). d) Root-mean-square error (RMSE) of the OTOC or MQC peak position for the 9 candidate free energy surfaces shown in (b); lines are a Gaussian process fit. Error bars in all plots are 1σ CI except for the estimates of the PMF minimum which are shown with 2σ CI from bootstrapping.

against experimental data. We plot [Fig. 4(d), green] the RMSE in the 6- and 7-quantum coherence spectra peak positions between experiment and the set of PMF candidates. The minima of the MQC, QC, and simulation RMSEs agree to within error bars, the error bars are similar in size, and the learned PMF improves the MQC RMSE by a factor 4 compared to a bare MD calculation. These results validate both the precision and the accuracy of our OTOC learning technique.

OUTLOOK

This work introduces a new quantum-information-inspired framework for determining long-range distance constraints in NMR, with potentially broad applications. Long-range distance constraints have proven essential in many contexts in NMR [22], serving as "anchor points" in structural biology [19, 20, 40, 41]. In these works, they have been used to discriminate polymorphs or furnish critical restraints for intramolecular and intersubunit geometries inaccessible to local probes. Beyond biomolecular systems, they have been critical in validating structural models and connectivity in materials such as metal–organic frameworks [42].

OTOCs probe long-range information via the propagation of local polarization across an extended spin network and its sensitivity to weak local perturbations under time-reversal. This approach offers advantages over traditional time-ordered correlation (TOC) experiments, i.e. protocols that do not involve time-reversal. Specifically, OTOCs may provide improved sensitivity to spatial correlations and distances in systems where local control is limited [26], such as the ^{13}C-proton networks studied within this work. While the size of the many-body correlations and the accessible distance measurements will be system-specific [43], these factors do not change the core applicability of the technique. Estimates (see Supplementary Information) suggest accessible distances of 20-60 Å for OTOC-based measurements, approaching the length scale of Förster Resonance Energy Transfer (FRET) [44]. This is beyond the reach of state of the art NMR techniques such as proton-driven spin diffusion (PDSD) [13], rotational echo double resonance (REDOR) [11], and radio-frequency-driven recoupling (RFDR) [12], all of which are TOC protocols.

Additionally, while the experiments presented here focus on single OTOCs, the framework naturally fits within the scope of multi-dimensional NMR. Multiple OTOCs, excited at distinct molecular sites or under effective Hamiltonians with varying symmetry-selection rules, could enable multi–anchor-point spectroscopy, supporting extensive extraction of structural parameters. Moreover, OTOCs need not be restricted to pulse-sequence excitation: molecular dynamics themselves may drive butterfly operations, providing access to distinct dynamical timescales and rendering the OTOC a direct probe of molecular motion [45]. The ability of quantum computers to simulate all of these potential experiments opens up future possibilities far beyond the studies undertaken in this work.

Despite the large body of work on the asymptotic analysis of product formulas [35], less work has gone into the constant factor analysis at beyond-classical system sizes.

The performance of product formula techniques [36, 46–49] can be highly system- and quantity-specific, and metrics such as unitary infidelity are only loose predictors of state- and operator-specific quantities such as OTOCs (see Supplementary Information). Estimates of Trotter errors suggest that naive methods would require $10^5 - 10^6$ gates to execute OTOCs on 50-spin systems (see Supplementary Information) — a large, but not astronomical gap to current hardware requirements given careful problem selection. This presents a challenge to the quantum algorithms community, as we do not expect this gap to be overcome by physical hardware alone.

Our application of the AlphaEvolve algorithm [5] presents an interesting new direction for such algorithm optimization research. Despite successfully overcoming the Trotterization challenge for DMBP, our AlphaEvolve optimization loop relies on evaluating candidate circuits against a complete, classically pre-computed dataset of OTOCs, which is not immediately scalable to beyond-classical system sizes. However, in this work we leveraged the inherent strengths of the LLM-based agent to write code that constructs Trotterized circuits, rather than generating circuits directly [50]. We argue that this has two key advantages. The first advantage is that the resulting code can generate circuits for times and landscape parameters outside its training data set, allowing some degree of generalization and protection against overfitting. However, while interpolation between the training data points works in limited cases, the generator commonly fails to extrapolate; improving on this is a key target for future research. The second advantage is that the resulting function and the prompts used can be understood and analysed by humans, which we attempt in the Supplementary Information. We find that the primary focus of the code (relative to a first order Trotter formula) is a mixture of light cone pruning, term and qubit ordering, adaptive time steps and a distance-based term rescaling, some of which have been suggested before in the literature [46, 48]. We suggest that such analysis can allow the ideas identified by AlphaEvolve to be scaled to system sizes inaccessible to exact simulation.

Molecular dynamics estimates are compromised by several sources of error, including finite size effects, force field inaccuracy, and insufficient sampling. While each of these issues may be addressed in principle, simultaneously addressing all of them is impractical. Instead, addressing these shortcomings through Hamiltonian learning represents a promising avenue for accurately assessing structural properties, enabled by scalable reproduction of many-body spin dynamics by quantum computers. Despite the limitations of the current scheme, in part due to experimental uncertainty, the learned mean value of the DMBP dihedral angle improves over predictions from condensed phase molecular mechanics. These results highlight that experimentally obtained quantum many-body echoes can parameterize highly tuned structural models by providing information that can correct the deficiencies of molecular dynamics simulations.

MATERIALS AND METHODS

Materials

Nematic liquid crystals 4'-Ethoxybenzylidene-4-butylaniline (≥99.0%) [EBBA] and 4-Cyano-4'-pentylbiphenyl (≥98.0%) [5CB] were purchased from Tokyo Chemical Industry America and used as received. Isotopically enriched [4-^{13}C]-toluene (≥99.0%) was purchased from Sigma Aldrich and used without further purification. Isotopically labeled samples of [1-^{13}C]-3',5'-dimethylbiphenyl and 3',5'-bis(methyl-d_3)biphenyl were synthesized according to literature procedures using starting materials purchased from Sigma-Aldrich; full synthetic details are provided in the Supplementary Information. The purity of synthesized [1-^{13}C]-3',5'-dimethylbiphenyl and [1-^{13}C]-3',5'-bis(methyl-d_3)biphenyl was confirmed by ^{1}H and ^{13}C NMR spectroscopy, showing no detectable impurities.

NMR sample preparation

[4-^{13}C]-toluene was prepared by mixing 4.2 wt% of the compound with EBBA, heating to 358 K to reach the isotropic phase, and sonicating to homogenize. [1-^{13}C]-3',5'-dimethylbiphenyl and 3',5'-bis(methyl-d_3)biphenyl were prepared by mixing 2% v/v of each compound with 5CB, followed by heating to 313 K and sonication. Prior to each NMR experiment, all samples were homogenized by sonication above the nematic–isotropic transition temperature, injected into the NMR magnet, thermally cycled several times through the transition point, and then cooled slowly to the target experimental temperature.

NMR experiments

NMR experiments were performed on a Bruker UltraShield 11.75 T (500 MHz for ^{1}H) magnet equipped with a Bruker Avance I console. A 5 mm double-resonance BBO smart probe was tuned to facilitate ^{1}H and ^{13}C experiments. The sample temperature was maintained at 295 K for [4-^{13}C]-toluene@EBBA and 289 K for [1-^{13}C]-3',5'-dimethylbiphenyl@5CB, [1-^{13}C]-3',5'-bis(methyl-d_3)biphenyl@5CB using the internal temperature control unit. Pulse powers of the ^{1}H and ^{13}C channels were synchronized to achieve a nutation amplitude of $\sim$ 23.8 kHz. All OTOC experiments were preceded by a preparation filter generating pure ^{13}C magnetization via a combination of gradient pulses and Loschmidt echo elements, followed by the application of a TARDIS element for variable durations. The TARDIS element was designed to generate effective dipolar double-quantum evolution in the presence of homo- and heteronuclear dipolar couplings

($H_{\text{eff}} \propto \sum_{i<j} d_{ij}^{II} I_i^+ I_j^+ + \sum_{i,j} d_{ij}^{IS} I_i^z S_j^z$ + h.c.), taking into account finite pulse width and pulse amplitude effects (see Supplementary Information). A selective perturbation, in the form of a local rotation, was applied to the methyl protons in both target systems. This was achieved through the application of a BLEW12 [51] element applied to the proton channel, resonant with the methyl spins, followed by a second BLEW12 proton element sandwiched by two carbon π-pulses. Time-reversal was achieved through a second $(\pi/2)$-phase-shifted TARDIS element sandwiched by two π pulses on the carbon channel. Application of the $(\pi/2)$-phase-shift reversed the sign of the double-quantum part of the effective generator ($R_z^I(\pi/2) I_i^+ I_j^+ R_z^I(-\pi/2) = -I_i^+ I_j^+$) [10], whereas the two π pulses on the carbon channel inverted the sign of the heteronuclear part similar to a spin echo. Finally, readout was performed on the ^{13}C channel. MQC spectroscopy followed the general scheme outlined in [34]. Full details of the NMR experiments and all pulse sequence elements are given in the Supplementary Information.

Processing of NMR and SC experimental data for learning experiments

Each NMR dataset shown is an average over 10 independent measurements, allowing us to calculate the standard error $\sigma_t = [\sum_j (C(t) - C_j(t))^2]^{1/2}/N$. Measurements of datapoints at different times were assumed to be independent. However, as the measured peak amplitudes are normalized by the OTOC at $t = 0$, the uncertainty in this amplitude was propagated to the other OTOC estimates, which led to a covariance matrix Σ_{NMR} with non-zero off-diagonal terms. Σ_{NMR} was then used to obtain the covariance weighted error plotted in Fig. 2(e): $\text{Cov. wt. err} = [(\boldsymbol{C}_{\text{NMR}} - \boldsymbol{C}_{\text{sim}})^T \Sigma_{\text{NMR}} (\boldsymbol{C}_{\text{NMR}} - \boldsymbol{C}_{\text{sim}})]^{1/2}/\text{Trace}[\Sigma]^{1/2}$. Here, we write $\boldsymbol{C}$ as shorthand for arrays containing the OTOC data indicated in the subscript. Error bars in Fig. 2(e) were obtained by bootstrapping over the initial 10 points for each NMR dataset. To combine this data with the output of the quantum computer for Fig. 3 and Fig. 4, we took the covariance matrix Σ_{QC} (which we assume to be diagonal), and combined this with the NMR covariance matrix to yield $\Sigma_{\text{tot}} = [\Sigma_{\text{NMR}}^{-1} (\Sigma_{\text{NMR}}^{-1} + \Sigma_{\text{QC}})^{-1} \Sigma_{\text{QC}}^{-1}]^{-1}$. This was substituted for Σ_{NMR} in the above definition of the covariance weighted error to give the cost function in Fig. 3(c). Error bars in this figure were calculated by bootstrapping over the NMR datapoints, and re-sampling the quantum computer data from a normal distribution. For Fig. 4(d), we used the root-mean-square error $\text{RMSE} = [\frac{1}{N} \|\boldsymbol{C}_{\text{sim}} - \boldsymbol{C}_{\text{NMR}}\|]^{1/2}$ as a cost function instead of the covariance weighted error.

Molecular dynamics simulations details

Starting structures were generated with Packmol version 21.0.0 [52] at a concentration of 2.05% v/v 1,3-dimethyl-5-(phenyl-13C)benzene and a starting density of 1.01 g/ml. The liquid crystal molecules were approximately aligned along the x-axis of the simulation box with dimensions [65Å, 50Å, 50Å] by providing angle constraints in the Packmol input file. The initial structures were then relaxed by minimizing the system at constant volume and equilibrated with 500 ps of isothermal-isobaric (NPT) dynamics. All simulations used a 2 fs time step with hydrogen bond constraints and a hydrogen mass of 4 amu. NPT calculations used a Monte Carlo barostat with updates every 25 steps. All ensemble averages were evaluated with respect to 8 independent trajectories with production times of 1 μs each. All molecular dynamics simulations were performed using OpenMM [53].

Non-bonded parameters from GAFF version 2.11 [54] were deployed for 5CB and DMBP in combination with bonded parameters from Grappa version 1.3.1 [55]. Although Grappa was designed for biomolecules, the training set includes a very large dataset of small organic molecules and we have observed empirically that the Grappa force field imparts additional flexibility to the aliphatic chains in the liquid crystal relative to GAFF. This is consistent with modifications made to GAFF for liquid crystal systems [56].

The order parameters of 5CB are known to be sensitive to the temperature [57, 58], and are difficult to model with molecular dynamics [59]. This necessarily impacts both the mean-value of the dihedral angle of DMBP, and the ϕ-dependent coupling matrices $D_{ij}(\phi)$. To minimize this effect, we shift the temperature of the experiment to 289 K (as reported in the above section), where the order parameters most accurately match simulation, and use this throughout all DMBP experiments.

Classical simulation of toluene

Toluene in EBBA was modeled as a static benzene ring with a freely rotating methyl group in a fixed plane, in a similar manner to Ref. [34]. The motion in the liquid crystal background was treated with the Saupe tensor formalism, assuming all molecular motion occurs on timescales $\ll 1$ ms (see Supplementary Information). Data for the molecular co-ordinates and all J-couplings was taken from Ref. [34], except for the J-coupling between the ^{13}C and the nearest proton (which is significantly larger than all other J-couplings). The Saupe tensor, chemical shifts, and the remaining J coupling were obtained by fitting to MQC data (see Supplementary Information). Data was separately validated by comparing to the molecular dynamics simulations of the toluene-EBBA system above.

Trotterized Hamiltonian simulation and machine learning

AlphaEvolve setup

AlphaEvolve [5] is an evolutionary coding agent that leverages large language models (LLMs) to discover novel and efficient solutions for a variety of scientific problems. In this work, AlphaEvolve is used to generate a set of Python functions that produce quantum circuits approximating Hamiltonian evolution across an entire parameter landscape of time and Hamiltonian inputs, as opposed to optimizing individual quantum circuits or circuit parameters directly. The process was seeded with a human-written program (a first-order Trotter formula) that served as the initial solution to a given task. Through a process of mutation, evaluation, and selection, AlphaEvolve ultimately generated a population of programs that produce simulation circuits with significantly lower approximation error against the reference (improving from a 10.4% mean error to 0.82%), while remaining below the gate budget enforced by the device (see Supplementary Information for further explanation).

The MAP-Elites-like setup of AlphaEvolve [60] was used as a base for this work, optimized for a single RMS error metric targeting the average approximation error across the entire set of landscape parameter and time values evaluated. By stochastically injecting domain-specific suggestions into the prompt, the optimization algorithm was steered towards granular changes relevant to the task. Here, task-specific modifications were introduced, such as a mixture of hand-crafted and LLM-generated task instructions specific to quantum simulation and circuit optimization problems. These led to increased performance of the algorithm, both in terms of achieved metric value and convergence speed, i.e. number of required LLM samples. The LLMs are pre-trained on large corpora of scientific literature and thus already possess knowledge of the most commonly used quantum algorithms, quantum simulation, and other relevant domain knowledge.

For each parent program, in addition to the program's overall RMS error, an associated error matrix was included in a tabular format giving the OTOC error for each point in the parameter landscape and time. This feedback allows the LLM to perform in-context reinforcement learning: by focusing on regions with high error, the model can attempt to generate a more accurate circuit for these regions without sacrificing overall performance.

The algorithm's parallelized nature was leveraged to redistribute resources. To cover a larger portion of the search space, multiple, initially independent AlphaEvolve runs were started. As the optimization progresses, the independent runs were regularly synced by re-seeding with the current best solution. This was either performed via full re-seeding or by eliminating only the worst-performing run. Empirically, we found that this strategy resulted in a much faster improvement of the fitness function with respect to the number of LLM samples used.

Circuit optimization problem setup

For processing by AlphaEvolve, a problem needs to be split into four well-defined pieces, as described here:

Problem Specification: A Python program implementing a first-order Trotter formula with a swap network for 15 qubits on a chain in a dense brick-wall fashion served as starting point for the evolutionary process. For this initial program, the input parameters of the function were the total time t and number of Trotter steps to be implemented, as well as the homogeneous/heterogeneous (j) couplings and an on-site terms. Additionally, we provided the butterfly and measurement indices, the landscape parameter p, and a maximum number of allowed CZ gates, despite these being unused in the function initially. These additional parameters were included in the function signature to inform AlphaEvolve about the wider context of the program, and to give additional information could be useful for optimization.

Prompt and sampling: In each iteration, AlphaEvolve selected a program from its database to act as a parent. This parent program was then used to generate a prompt for an LLM, which was tasked with creating a child program that improves upon the parent. A fixed generic prompt was included, describing quantum simulation, Trotterization, NMR, and OTOCs on a very high level. Per LLM call, a domain-specific or generic prompt was further added, as well as focus prompts that primarily target code simplification, refactoring and removal of dead code, or to focus on a particular task (lightcone, THRIFT [61], commutator scaling). In all cases, the signature of the function to be generated remained fixed.

Evaluation: The obtained function was used to generate quantum circuits for all choices of parameters and time steps. These circuits were then individually evaluated by averaging the OTOC over 250 randomly-sampled initial states. To ensure that this random evaluation yields only a small approximation error, this approximate OTOC was compared with the exact OTOC computation that uses the full set of 2^{15} states. For the latter a new technique using sparse matrix computations on GPU was implemented to produce unitary matrices for large circuits instead of much slower regular einsum-based method. The seed for the state sampling varied for each time and landscape parameter choice, but remained fixed throughout the optimization run to avoid small random fluctuations influencing the evaluation of mutations while speeding up the pipeline. The root mean square error between the evaluated OTOCs and the reference data was used as an optimization metric.

Database Integration: Child programs that were both valid and exhibited a sufficiently high fitness score were added to the database of programs. Programs were discarded, for example, if the circuit they produced ex-

ceeded a predefined number of gates. Counting CZ gates as implemented in the Cirq framework with Cartan's KAK decomposition [62] was the dominant bottleneck, with this calculation alone being the dominant part of the step time. To optimize this, a highly parallel KAK decomposition was implemented, effectively removing the contribution of the compilation step to the total time and compute budget. Consequently, the evolved program was provided with an option to use CZ counting as a tool (which it did by implementing a two-pass circuit generation, see Supplementary Information).

We provide an additional analysis on the efficiency of different instruction prompts, high-level intuition of what kinds of modifications AlphaEvolve suggests and generated codes and circuits in the Supplementary Information.

Details of superconducting qubit devices and gate calibration

Quantum simulation was performed on a Willow quantum computer similar to that described in [4] (see also [63]). Processors in this lineage are based on a 2D grid of flux tunable superconducting transmon qubits connected by flux tunable couplers between nearest neighbors. In this work, the mean frequency of operation was ~ 6.2 GHz with anharmonicity $\sim$210 MHz.

As the two molecules addressed in this work require nine and fifteen qubits only, we selected a sub-grid of the 105 qubit Willow with performance better than average in the relevant benchmark metrics. Qubits were arranged in a line, with the measurement qubit at one end. The average lifetime of the single photon excitation in the chosen line of qubits was $T_1 = 114$ µs. The average coherence time of the chosen qubits as measured by a Hahn-Echo sequence was $T_{2E} = 130$ µs. The performance of single qubit microwave gates was measured by Clifford randomized benchmarking (RB) error and the associated qubit impurity, which were found to be on average 0.00020 and 0.00015, respectively. The average cycle Pauli cross-entropy benchmarking (XEB) error, including error contributions from two single qubit gates and a single two-qubit gate, was for CZ 0.0015, and for $\sqrt{i\text{SWAP}}$ 0.0014. The average readout error of the single measurement qubit was 0.00985. Since the data taking for the quantum simulation of the OTOC-NMR learning sequence took several days, these metrics drifted slightly before completion. While the processor requires recalibration during this time, these numbers are typical and representative of our experiments.

The all-to-all coupling was achieved by a swap network, a technique adapted from [37]. Here, one compiles swap gates through a depth N "brick wall" pattern of two-qubit interactions, such that the swap gates permute floating spin indices through the qubit array. This is optimal in terms of both the number of gates and the depth required to execute one interaction between each pair of spins, as is needed for a single Trotter step of the all-to-all coupled dipolar Hamiltonian. In our quantum simulation of Toluene, we further approximated that the ^{13}C spin only interacted with its nearest proton. This single coupling was treated in the interaction frame and the ^{13}C spin was removed from the swap network, reducing the number of gates needed by 17%. This approximation was justified as all other ^{1}H-^{13}C couplings were two orders of magnitude smaller for the entire set of toluene geometries considered, and we observed that the interaction frame treatment slightly reduced the Trotter error.

The quantum simulation for Toluene was based on a natural decomposition of the target effective Hamiltonian into Fermionic simulation (fSim) gates [64]. These gates are parametrized by two two-qubit interaction angles: the swap angle and the conditional phase angle. Across the entire landscape, the Trotterization of the Toluene evolution required calibrating a set of 80 unique fSim gates. Previous work was able to operate with a single pulse fSim [3, 65–69]. However, achieving arbitrary combinations of swap and conditional phase angles with a single pulse often requires either a long gate duration, which degrades performance by decoherence, or a large interaction coupling strength between qubits, which increases leakage processes outside of the computational manifold. In this work, due to the range of coupling strengths in Toluene and the coarse-grained Trotterization, the swap angles that needed to be calibrated spanned the entire domain from 0 to $\pi/2$. To solve this issue, we adapted a two-pulse fSim approach from earlier work in a Sycamore architecture [64]. Here, a first base band interaction pulse sets the swap angle and induces a spurious < 100 mrad conditional phase, while a second pulse enacts a conditional phase and a spurious ~ 30 mrad swap angle. The two-pulse approach is calibration intensive, but provides higher performance and flexibility than a single pulse approach.

The two pulses for each fSim gate were calibrated together as a single gate with an iterative procedure adapting one of two high precision periodic "Floquet" calibrations previously developed, depending on the target swap angle. For small target swap angles (< 30 mrad) we adapted the technique presented in [66]. For larger swap angles and for the conditional phase we adapted the technique presented in [65]. To achieve the desired precision in the full range we fine-tuned the number of gates used in the periodic calibration and fitting procedure depending on the value of the expected angle. The procedure accounts for the aforementioned spurious terms as part of the calibrated final gate, attaining the target interaction angles with a max tolerance of 20 mrad, and typical error < 5 mrad. As in previous work [3, 4], single qubit phases of the fSim gates are measured by XEB fitting and removed by phase matching single qubit gates to yield the total gate. The median XEB error for the tuned fSim gates was measured at 0.0026 and max XEB error 0.0045. Compatible pairs of qubits were calibrated simultaneously, and therefore benchmarks include cross-

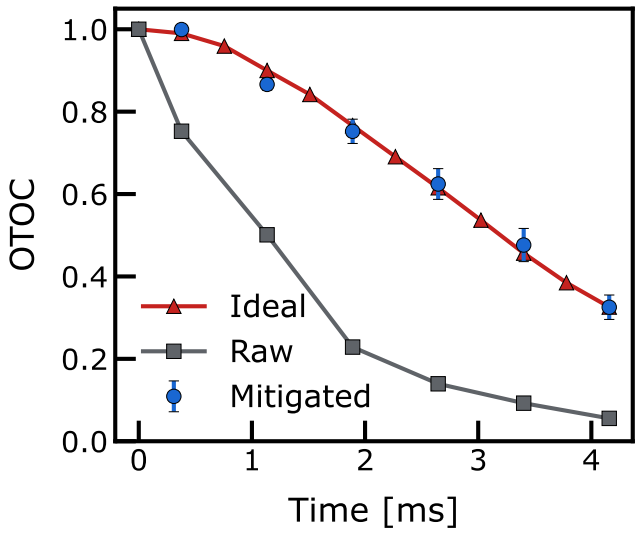

Extended Data Fig. 1. Benchmark of Pauli Path ZNE error mitigation on the 15-spin molecule at odd time indices. Out-of-time-order correlator (OTOC) measurements for DMBP at *odd* NMR time indices, taken during a different experimental run from that shown in the main text, on a different date, to provide a secondary benchmark. The smallest raw signal (gray squares) measured was 0.055 ± 0.003 (data includes real-time readout mitigation, double-sided light cone filtering, twirling, and dynamical decoupling). Despite this small signal, the Pauli Path ZNE-mitigated data (blue circles) was successfully extracted, serving as a stringent test for the mitigation technique.

talk effects. More details on these experiments can be found in the Supplementary Information.

For the quantum simulation of DMBP, a 15 qubit linear chain with similar performance was used. In contrast to the Toluene experiments, the AlphaEvolve coding agent generated circuits using a CZ decomposition, which did not require us to use the fSim construction detailed above.

Error mitigation pipeline for noisy quantum circuits

The structured character of the NMR OTOC circuits prohibits the use of mitigation strategies used in earlier works that are tailored to random OTOC circuit ensembles [4]. The circuits used are also very deep: the deepest 9-spin circuits span 326 circuit moments and used 540 two-qubit composite fSim gates, while the deepest circuits for the 15-spin molecule span 484 moments and used 792 CZ gates. (These numbers count only relevant gates within the double light cones of the measurement and butterfly operators; we typically remove gates that will have no impact on the final OTOC measurement from the circuit.) The resulting damping of the noisy OTOC signal was observed in the worst case to be as small as 0.15.

To reliably and accurately extract data from these noisy quantum circuits, we employ a composite, reconfigurable error mitigation framework designed to operate across different gate sets, using distinct configurations for the 9-spin (fSim-based) and 15-spin (CZ-based) molecular OTOC experiments. We developed a four-stage mitigation pipeline consisting of algorithmic and physical-level stages: (1) Circuit generation at the algorithmic level; (2) Algorithmic-level error mitigation, which involved double-sided light cone filtering [4], Pauli Path ZNE (described below) [70–73], algorithmic-level DD, and sub-Clifford algorithmic-block twirling [74, 75]; (3) Native gate decomposition and optimization; (4) Physical-layer mitigation, which involved hardware-adapted DD sequences for idle periods with Clifford twirling [74–77], and real-time randomized readout error mitigation [78]. This describes the full pipeline for the 9 spin fSim circuits. The 15 spin CZ-based circuit used the same pipeline, but without the need for algorithmic-level DD, and using full (rather than sub) Clifford group twirling for the two-qubit gates and idle periods.

As part of this work, we developed a novel Pauli-path zero-noise extrapolation (ZNE) scheme based on the evolution of the measurement operator in the Pauli path picture [3, 4, 30, 79]. This is based on the identification that the noisy expectation value $C(\lambda)$ (with λ the noise scaling factor) is the Laplace transform of the underlying Pauli path total Hamming weight distribution $c(H)$ [4], where H is the noise accumulation weight. Though this distribution $c(H)$ can be highly oscillatory, the Laplace transform smooths out high-frequency components, allowing simple, low frequency approximations to $c(H)$ to robustly extrapolate $C(\lambda)$. Taking a normal approximation of $c(H)$, we derive an analytical functional form for the observed decay which serves as our main model for extrapolation:

$$C(\lambda) = C(0)\frac{\left(1+\mathrm{erf}(\frac{\bar{H}_c-\lambda\sigma_c^2}{\sigma_c})\right)}{\left(1+\mathrm{erf}(\bar{H}_c/\sigma_c)\right)} e^{-\lambda\bar{H}_c} e^{\lambda^2\sigma_c^2/2}\,. \qquad (2)$$

The functional form is parameterized by three key quantities: $C(0)$ is the noise-free extrapolated value, while $\bar{H}_c$ and σ_c represent the mean and standard deviation respectively of the Pauli path Hamming weight distribution $c(H)$. These two parameters effectively characterize the noise-induced decay profile. We define the dimensionless parameter β as the ratio of the spread to the average noise accumulation $\beta = \frac{\sigma_c}{\bar{H}_c}$, where $\beta > 0$ and typically $\beta < 0.5$. For deep circuits where β is non-negligible, the quadratic term $e^{\lambda^2\sigma_c^2/2}$ and the error function (erf) correction become essential, as they account for the non-exponential, concave decay profile caused by the complex quantum dynamics, and the physical constraint of non-negative noise weight ($H \geq 0$). This model is conjectured to work even in the regime where Pauli path numeric approximations fail (as is the case in these experiments).

The Pauli Path ZNE framework can be very sensitive to statistical noise when working with deep circuits with

low fidelities. To achieve robust extrapolation across the entire time series, we implemented a specialized Bayesian model-fitting update workflow. This time-correlated strategy utilizes data from shallower, less-noisy time steps—where the circuit fidelity is stronger—to establish a Bayesian prior. This prior then iteratively seeds and updates the model fit for deeper, noisier circuits, stabilizing the parameter estimation for the extrapolation. We employ a global-parameter optimization algorithm, which combines a local minimization routine with random jumps across the parameter space to overcome local optimization minima and improve robustness to noise, and a rare outlier rejection protocol. We employ bootstrap resampling over the mitigation circuit instances to evaluate both the mitigated values and their respective uncertainties. This combined with the Pauli path theory allows the system to overcome the challenges associated with signal damping and accurately estimate the zero-noise limit even in the deepest regions of the circuit.

ACKNOWLEDGMENTS

The authors acknowledge useful discussions with L. Emsley, L.D. Nielsen, T. Polenova, R. Schurko, R. Tycko, G. Pantaleoni, and N. Wiebe. We thank Pines Magnetic Resonance Center's Core NMR Facility at UC Berkeley for spectroscopic resources used in this study. D.W. Berry worked on this project under a sponsored research agreement with Google Quantum AI.

AUTHOR CONTRIBUTIONS

C. Zhang prepared molecular samples and performed the NMR experiments. R.G. Cortiñas and A.H. Karamlou performed the superconducting quantum simulation experiments. C. Zhang, C. Bengs, C. Ramanathan, A. Ajoy, and T.E. O'Brien conceived of the NMR OTOC experiments. C. Zhang and C. Bengs designed the pulse sequence elements and selected the molecular systems. S.H. Kang and R. Sarpong synthesized isoptically-enriched samples of DMBP. J. Provazza, N.C. Rubin, and A. White performed molecular dynamics simulations of the 9Q and 15Q experiments and conceived of the learning experiment. N.C. Rubin, C. Zhang, C. Bengs, J. Provazza, A. White, and T.E. O'Brien performed noisy density matrix simulations of the toluene and DMBP experiments. R.G. Cortiñas, X. Mi, and T.E. O'Brien designed the circuits for the 9-qubit superconducting experiment. J. Bausch, S. Shirobokov, A. Senior, N. Tomašev, B. Kozlovskii, F.J.H. Heras, and P. Kohli designed, tested, and ran the AlphaEvolve optimization experiments. R.G. Cortiñas designed and implemented the pulse calibration sequence for the arbitrary-angle fSim gate, with assistance from X. Mi and J.A. Gross. Z.K. Minev, N. Noll, R.G. Cortinãs, A.H. Karamlou and T.E. O'Brien implemented the coding infrastructure for the superconducting experiments. N. Noll, D. Kafri and Z.K. Minev performed accurate modeling of the superconducting qubit experiments. Z.K. Minev and N. Noll designed and implemented the error mitigation sequences with assistance from T.E. O'Brien and T. Schuster. The Google Quantum AI team designed, built, calibrated and maintained the superconducting qubit chip, along with the dilution refrigeration, the electronics stack, and the superconducting experiment codebase. All authors contributed to the writing and revisions of the manuscript.

[1] Igor L. Aleiner, Lara Faoro, and Lev B. Ioffe, "Microscopic model of quantum butterfly effect: Out-of-time-order correlators and traveling combustion waves," Ann. Phys. **375**, 378–406 (2016).

[2] Daniel A. Roberts, Douglas Stanford, and Leonard Susskind, "Localized shocks," J. High Energy Phys. **2015**, 51 (2015).

[3] Xiao Mi, Pedram Roushan, Chris Quintana, Salvatore Mandra, Jeffrey Marshall, Charles Neill, Frank Arute, Kunal Arya, Juan Atalaya, Ryan Babbush, Joseph C. Bardin, Rami Barends, Andreas Bengtsson, Sergio Boixo, Alexandre Bourassa, Michael Broughton, Bob B. Buckley, David A. Buell, Brian Burkett, Nicholas Bushnell, Zijun Chen, Benjamin Chiaro, Roberto Collins, William Courtney, Sean Demura, Alan R. Derk, Andrew Dunsworth, Daniel Eppens, Catherine Erickson, Edward Farhi, Austin G. Fowler, Brooks Foxen, Craig Gidney, Marissa Giustina, Jonathan A. Gross, Matthew P. Harrigan, Sean D. Harrington, Jeremy Hilton, Alan Ho, Sabrina Hong, Trent Huang, William J. Huggins, L. B. Ioffe, Sergei V. Isakov, Evan Jeffrey, Zhang Jiang, Cody Jones, Dvir Kafri, Julian Kelly, Seon Kim, Alexei Kitaev, Paul V. Klimov, Alexander N. Korotkov, Fedor Kostritsa, David Landhuis, Pavel Laptev, Erik Lucero, Orion Martin, Jarrod R. McClean, Trevor McCourt, Matt McEwen, Anthony Megrant, Kevin C. Miao, Masoud Mohseni, Wojciech Mruczkiewicz, Josh Mutus, Ofer Naaman, Matthew Neeley, Michael Newman, Murphy Yuezhen Niu, Thomas E. O'Brien, Alex Opremcak, Eric Ostby, Balint Pato, Andre Petukhov, Nicholas Redd, Nicholas C. Rubin, Daniel Sank, Kevin J. Satzinger, Vladimir Shvarts, Doug Strain, Marco Szalay, Matthew D. Trevithick, Benjamin Villalonga, Theodore White, Z. Jamie Yao, Ping Yeh, Adam Zalcman, Hartmut Neven, Igor Aleiner, Kostyantyn Kechedzhi, Vadim Smelyanskiy, and Yu Chen, "Information scrambling in computationally complex quantum circuits," Science **374**, 1479 (2021).

[4] Google Quantum AI and Collaborators, "Constructive interference at the edge of quantum ergodic dynamics,"

arXiv:2506.10191 (2025).
[5] Alexander Novikov, Ngân Vũ, Marvin Eisenberger, Emilien Dupont, Po-Sen Huang, Adam Zsolt Wagner, Sergey Shirobokov, Borislav Kozlovskii, Francisco J. R. Ruiz, Abbas Mehrabian, M. Pawan Kumar, Abigail See, Swarat Chaudhuri, George Holland, Alex Davies, Sebastian Nowozin, Pushmeet Kohli, and Matej Balog, "Alphaevolve: A coding agent for scientific and algorithmic discovery," (2025), arXiv:2506.13131 [cs.AI].
[6] Malcolm H Levitt, *Spin dynamics: basics of nuclear magnetic resonance* (John Wiley & Sons, 2008).
[7] Hyungjoon Cho, Thaddeus D Ladd, Jonathan Baugh, David G Cory, and Chandrasekhar Ramanathan, "Multispin dynamics of the solid-state nmr free induction decay," Physical Review B—Condensed Matter and Materials Physics **72**, 054427 (2005).
[8] Mark C Butler, Jean-Nicolas Dumez, and Lyndon Emsley, "Dynamics of large nuclear-spin systems from low-order correlations in liouville space," Chemical Physics Letters **477**, 377–381 (2009).
[9] Jean-Nicolas Dumez, Meghan E Halse, Mark C Butler, and Lyndon Emsley, "A first-principles description of proton-driven spin diffusion," Physical Chemistry Chemical Physics **14**, 86–89 (2012).
[10] J. Baum, M. Munowitz, A. N. Garroway, and A. Pines, "Multiple-quantum dynamics in solid state NMR," The Journal of Chemical Physics **83**, 2015–2025 (1985).
[11] Terry Gullion and Jacob Schaefer, "Rotational-echo double-resonance nmr," Journal of Magnetic Resonance (1969) **81**, 196–200 (1989).
[12] Andrew E Bennett, Chad M Rienstra, Janet M Griffiths, Weiguo Zhen, Peter T Lansbury Jr, and Robert G Griffin, "Homonuclear radio frequency-driven recoupling in rotating solids," The Journal of chemical physics **108**, 9463–9479 (1998).
[13] M.G. Colombo, B.H. Meier, and R.R. Ernst, "Rotor-driven spin diffusion in natural-abundance 13c spin systems," Chemical Physics Letters **146**, 189–196 (1988).
[14] Andreas Grommek, Beat H. Meier, and Matthias Ernst, "Distance information from proton-driven spin diffusion under mas," Chemical Physics Letters **427**, 404–409 (2006).
[15] D. P. Raleigh, F. Creuzet, S. K. Das Gupta, M. H. Levitt, and Robert G. Griffin, "Measurement of internuclear distances in polycrystalline solids. rotationally enhanced transfer of nuclear spin magnetization," Journal of the American Chemical Society **111**, 4502–4503 (1989), https://doi.org/10.1021/ja00194a057.
[16] F. Creuzet, A. McDermott, R. Gebhard, K. van der Hoef, M. B. Spijker-Assink, J. Herzfeld, J. Lugtenburg, M. H. Levitt, and R. G. Griffin, "Determination of membrane protein structure by rotational resonance nmr: Bacteriorhodopsin," Science **251**, 783–786 (1991), https://www.science.org/doi/pdf/10.1126/science.1990439.
[17] W. S. Warren and A. Pines, "Analogy of multiple-quantum nmr to isotopic spin labeling," Journal of the American Chemical Society **103**, 1613–1617 (1981), https://doi.org/10.1021/ja00397a001.
[18] James M. Polson and E. Elliott Burnell, "Conformational equilibrium and orientational ordering: 1h-nuclear magnetic resonance of butane in a nematic liquid crystal," The Journal of Chemical Physics **103**, 6891–6902 (1995).
[19] Aneta T Petkova, Yoshitaka Ishii, John J Balbach, Oleg N Antzutkin, Richard D Leapman, Frank Delaglio, and Robert Tycko, "A structural model for alzheimer's β-amyloid fibrils based on experimental constraints from solid state nmr," Proceedings of the National Academy of Sciences **99**, 16742–16747 (2002).
[20] Christian Wasmer, Adam Lange, Hélène Van Melckebeke, Ansgar B Siemer, Roland Riek, and Beat H Meier, "Amyloid fibrils of the het-s (218–289) prion form a β solenoid with a triangular hydrophobic core," Science **319**, 1523–1526 (2008).
[21] João Medeiros-Silva, Aurelio J. Dregni, Noah H. Somberg, Pu Duan, and Mei Hong, "Atomic structure of the open SARS-CoV-2 E viroporin," Science Advances **9**, eadi9007 (2023).
[22] Alexander A. Shcherbakov, João Medeiros-Silva, Nhi Tran, Martin D. Gelenter, and Mei Hong, "From Angstroms to Nanometers: Measuring Interatomic Distances by Solid-State NMR," Chemical Reviews **122**, 9848–9879 (2022).
[23] Dries Sels, Hesam Dashti, Samia Mora, Olga Demler, and Eugene Demler, "Quantum approximate bayesian computation for nmr model inference," Nature machine intelligence **2**, 396–402 (2020).
[24] Thomas E O'Brien, Lev B Ioffe, Yuan Su, David Fushman, Hartmut Neven, Ryan Babbush, and Vadim Smelyanskiy, "Quantum computation of molecular structure using data from challenging-to-classically-simulate nuclear magnetic resonance experiments," PRX Quantum **3**, 030345 (2022).
[25] Manuel G Algaba, Mario Ponce-Martinez, Carlos Munuera-Javaloy, Vicente Pina-Canelles, Manish J Thapa, Bruno G Taketani, Martin Leib, Inés De Vega, Jorge Casanova, and Hermanni Heimonen, "Co-design quantum simulation of nanoscale nmr," Physical Review Research **4**, 043089 (2022).
[26] Thomas Schuster, Murphy Niu, Jordan Cotler, Thomas O'Brien, Jarrod R McClean, and Masoud Mohseni, "Learning quantum systems via out-of-time-order correlators," Physical Review Research **5**, 043284 (2023).
[27] Kushal Seetharam, Debopriyo Biswas, Crystal Noel, Andrew Risinger, Daiwei Zhu, Or Katz, Sambuddha Chattopadhyay, Marko Cetina, Christopher Monroe, Eugene Demler, *et al.*, "Digital quantum simulation of nmr experiments," Science Advances **9**, eadh2594 (2023).
[28] Keith R Fratus, Nicklas Enenkel, Sebastian Zanker, Jan-Michael Reiner, Michael Marthaler, and Peter Schmitteckert, "Can a quantum computer simulate nuclear magnetic resonance spectra better than a classical one?" arXiv preprint arXiv:2508.06448 (2025).
[29] Michael Marthaler, Peter Pinski, Pascal Stadler, Vladimir Rybkin, and Marina Walt, "What is a good use case for quantum computers?" arXiv preprint arXiv:2506.15426 (2025).
[30] Armando Angrisani, Alexander Schmidhuber, Manuel S Rudolph, M Cerezo, Zoë Holmes, and Hsin-Yuan Huang, "Classically estimating observables of noiseless quantum circuits," arXiv preprint arXiv:2409.01706 (2024).
[31] Kostyantyn Kechedzhi, Sergei V Isakov, Salvatore Mandrà, Benjamin Villalonga, Xiao Mi, Sergio Boixo, and Vadim Smelyanskiy, "Effective quantum volume, fidelity and computational cost of noisy quantum processing experiments," Future Generation Computer Systems **153**, 431–441 (2024).
[32] Thomas Schuster, Chao Yin, Xun Gao, and Norman Y Yao, "A polynomial-time classical algorithm for noisy

quantum circuits," arXiv preprint arXiv:2407.12768 (2024).
[33] Jun Li, Ruihua Fan, Hengyan Wang, Bingtian Ye, Bei Zeng, Hui Zhai, Xinhua Peng, and Jiangfeng Du, "Measuring out-of-time-order correlators on a nuclear magnetic resonance quantum simulator," Physical Review X **7**, 031011 (2017).
[34] Leslie D Field and Saadallah A Ramadan, "Multiple quantum nmr spectra of toluene and p-bromotoluene partially aligned in a nematic phase," Magnetic Resonance in Chemistry **41**, 933–938 (2003).
[35] Andrew M Childs, Yuan Su, Minh C Tran, Nathan Wiebe, and Shuchen Zhu, "Theory of trotter error with commutator scaling," Physical Review X **11**, 011020 (2021).
[36] Guang Hao Low and Nathan Wiebe, "Hamiltonian simulation in the interaction picture," arXiv preprint arXiv:1805.00675 (2018).
[37] Ian D Kivlichan, Jarrod McClean, Nathan Wiebe, Craig Gidney, Alán Aspuru-Guzik, Garnet Kin-Lic Chan, and Ryan Babbush, "Quantum simulation of electronic structure with linear depth and connectivity," Physical review letters **120**, 110501 (2018).
[38] Kristan Temme, Sergey Bravyi, and Jay M Gambetta, "Error mitigation for short-depth quantum circuits," Physical review letters **119**, 180509 (2017).
[39] Ying Li and Simon C Benjamin, "Efficient variational quantum simulator incorporating active error minimization," Physical Review X **7**, 021050 (2017).
[40] Ann McDermott, "Structure and dynamics of membrane proteins by magic angle spinning solid-state nmr," Annual review of biophysics **38**, 385–403 (2009).
[41] Yun Han, Jinwoo Ahn, Jason Concel, In-Ja L Byeon, Angela M Gronenborn, Jun Yang, and Tatyana Polenova, "Solid-state nmr studies of hiv-1 capsid protein assemblies," Journal of the American Chemical Society **132**, 1976–1987 (2010).
[42] Xueqian Kong, Hexiang Deng, Fangyong Yan, Jihan Kim, Joseph A Swisher, Berend Smit, Omar M Yaghi, and Jeffrey A Reimer, "Mapping of functional groups in metal-organic frameworks," Science **341**, 882–885 (2013).
[43] Alexander Karabanov, Ilya Kuprov, G. T. P. Charnock, Anniek van der Drift, Luke J. Edwards, and Walter Köckenberger, "On the accuracy of the state space restriction approximation for spin dynamics simulations," The Journal of Chemical Physics **135**, 084106 (2011).
[44] L Stryer and R P Haugland, "Energy transfer: a spectroscopic ruler." Proceedings of the National Academy of Sciences **58**, 719–726 (1967), https://www.pnas.org/doi/pdf/10.1073/pnas.58.2.719.
[45] Alexey Krushelnitsky, Detlef Reichert, and Kay Saalwachter, "Solid-state nmr approaches to internal dynamics of proteins: from picoseconds to microseconds and seconds," Accounts of chemical research **46**, 2028–2036 (2013).
[46] Andrew M Childs, Aaron Ostrander, and Yuan Su, "Faster quantum simulation by randomization," Quantum **3**, 182 (2019).
[47] Earl Campbell, "Random compiler for fast hamiltonian simulation," Physical review letters **123**, 070503 (2019).
[48] Hongzheng Zhao, Marin Bukov, Markus Heyl, and Roderich Moessner, "Making trotterization adaptive and energy-self-correcting for nisq devices and beyond," PRX Quantum **4**, 030319 (2023).
[49] Refik Mansuroglu, Felix Fischer, and Michael J Hartmann, "Problem-specific classical optimization of hamiltonian simulation," Physical Review Research **5**, 043035 (2023).
[50] Linus Jern, Valter Uotila, Cong Yu, and Bo Zhao, "Agent-q: Fine-tuning large language models for quantum circuit generation and optimization," (2025), arXiv:2504.11109 [quant-ph].
[51] D.P Burum, M Linder, and R.R Ernst, "Low-power multipulse line narrowing in solid-state nmr," Journal of Magnetic Resonance (1969) **44**, 173–188 (1981).
[52] Leandro Martínez, Ricardo Andrade, Ernesto G Birgin, and José Mario Martínez, "Packmol: A package for building initial configurations for molecular dynamics simulations," Journal of computational chemistry **30**, 2157–2164 (2009).
[53] Peter Eastman, Raimondas Galvelis, Raúl P Peláez, Charlles RA Abreu, Stephen E Farr, Emilio Gallicchio, Anton Gorenko, Michael M Henry, Frank Hu, Jing Huang, *et al.*, "Openmm 8: molecular dynamics simulation with machine learning potentials," The Journal of Physical Chemistry B **128**, 109–116 (2023).
[54] Junmei Wang, Romain M Wolf, James W Caldwell, Peter A Kollman, and David A Case, "Development and testing of a general amber force field," Journal of computational chemistry **25**, 1157–1174 (2004).
[55] Leif Seute, Eric Hartmann, Jan Stühmer, and Frauke Gräter, "Grappa–a machine learned molecular mechanics force field," Chemical Science **16**, 2907–2930 (2025).
[56] Jianguo Zhang, Jiaye Su, and Hongxia Guo, "An atomistic simulation for 4-cyano-4'-pentylbiphenyl and its homologue with a reoptimized force field," The Journal of Physical Chemistry B **115**, 2214–2227 (2011).
[57] Roger G Horn, "Refractive indices and order parameters of two liquid crystals," Journal de physique **39**, 105–109 (1978).
[58] PL Sherrell and DA Crellin, "Susceptibilities and order parameters of nematic liquid crystals," Le Journal de Physique Colloques **40**, C3–211 (1979).
[59] Ivo Cacelli, Silvio Campanile, Giacomo Prampolini, and Alessandro Tani, "Stability of the nematic phase of 4-n-pentyl-4'-cyanobiphenyl studied by computer simulation using a hybrid model," The Journal of chemical physics **117**, 448–453 (2002).
[60] Jean-Baptiste Mouret and Jeff Clune, "Illuminating search spaces by mapping elites," (2015), arXiv:1504.04909 [cs.AI].
[61] Jan Lukas Bosse, Andrew M Childs, Charles Derby, Filippo Maria Gambetta, Ashley Montanaro, and Raul A Santos, "Efficient and practical hamiltonian simulation from time-dependent product formulas," Nat. Commun. **16**, 2673 (2025).
[62] Robert R. Tucci, "An introduction to cartan's kak decomposition for qc programmers," (2005), arXiv:quant-ph/0507171 [quant-ph].
[63] Rajeev Acharya, Laleh Aghababaie-Beni, Igor Aleiner, Trond I. Andersen, *et al.*, "Quantum error correction below the surface code threshold," Nature **638**, 920–926 (2025).
[64] Brooks Foxen, Charles Neill, Andrew Dunsworth, Pedram Roushan, Ben Chiaro, Anthony Megrant, Julian Kelly, Zijun Chen, Kevin Satzinger, Rami Barends, *et al.*, "Demonstrating a continuous set of two-qubit gates for near-term quantum algorithms," Physical Review Letters

125, 120504 (2020).

[65] Frank Arute, Kunal Arya, Ryan Babbush, Dave Bacon, Joseph C. Bardin, *et al.*, "Observation of separated dynamics of charge and spin in the Fermi-Hubbard model," Science Advances **6**, eaay5901 (2020), arXiv:2010.07965 [quant-ph].

[66] Xiao Mi, Matteo Ippoliti, Roderich Moessner, S. L. Sondhi, *et al.*, "Observation of time-crystalline eigenstate order on a quantum processor," Nature **601**, 53–57 (2022), arXiv:2107.13571 [quant-ph].

[67] Chris Neill, Tom McCourt, Xiao Mi, Zhang Jiang, Muqing Y. Niu, *et al.*, "Accurately computing the electronic properties of a quantum ring," Nature **594**, 508–512 (2021), arXiv:2012.00921 [quant-ph].

[68] Xiao Mi, Marius Sonner, Muqing Y. Niu, Kang W. Lee, Benjamin Foxen, Rajeev Acharya, Igor Aleiner, Trond I. Andersen, Frank Arute, *et al.*, "Noise-resilient edge modes on a chain of superconducting qubits," Science **378**, 785–790 (2022), arXiv:2204.11372 [quant-ph].

[69] Alexis Morvan, Trond I. Andersen, Xiao Mi, Charles Neill, *et al.*, "Formation of robust bound states of interacting microwave photons," Nature **612**, 240–245 (2022), arXiv:2206.05254 [quant-ph].

[70] Kristan Temme, Sergey Bravyi, and Jay M. Gambetta, "Error mitigation for short-depth quantum circuits," Physical Review Letters **119** (2016), 10.1103/PhysRevLett.119.180509.

[71] Ying Li and Simon C. Benjamin, "Efficient variational quantum simulator incorporating active error minimization," Physical Review X **7**, 021050 (2017).

[72] Zhenyu Cai, Ryan Babbush, Simon C. Benjamin, Suguru Endo, William J. Huggins, Ying Li, Jarrod R. McClean, and Thomas E. O'Brien, "Quantum error mitigation," Reviews of Modern Physics **95**, 045005 (2023), arXiv:2210.00921 [quant-ph].

[73] Zlatko K. Minev, Khadijeh Najafi, Swarnadeep Majumder, Juven Wang, Ady Stern, Eun-Ah Kim, Chao-Ming Jian, and Guanyu Zhu, "Realizing string-net condensation: Fibonacci anyon braiding for universal gates and sampling chromatic polynomials," Nature Communications **16**, 6225 (2025).

[74] Charles H. Bennett, Gilles Brassard, Sandu Popescu, Benjamin Schumacher, John A. Smolin, and William K. Wootters, "Purification of noisy entanglement and faithful teleportation via noisy channels," Physical Review Letters **76**, 722–725 (1995).

[75] E. Knill, "Fault-tolerant postselected quantum computation: Threshold analysis," arXiv e-prints , quant-ph/0404104 (2004), arXiv:quant-ph/0404104 [quant-ph].

[76] Lorenza Viola and Seth Lloyd, "Dynamical suppression of decoherence in two-state quantum systems," Phys. Rev. A **58**, 2733–2744 (1998), quant-ph/9803057.

[77] Lorenza Viola, Emanuel Knill, and Seth Lloyd, "Dynamical Decoupling of Open Quantum Systems," Phys. Rev. Lett. **82**, 2417–2421 (1999), quant-ph/9809071.

[78] Ewout van den Berg, Zlatko K. Minev, and Kristan Temme, "Model-free readout-error mitigation for quantum expectation values," Phys. Rev. A **105**, 032620 (2022).

[79] Manuel S Rudolph, Tyson Jones, Yanting Teng, Armando Angrisani, and Zoë Holmes, "Pauli propagation: A computational framework for simulating quantum systems," arXiv preprint arXiv:2505.21606 (2025).